

**Directional Spreading of Viscous Droplets on Wettability-patterned
Diverging Tracks**

by

Uddalok Sen
B.M.E. (Jadavpur University, India) 2014

Thesis submitted in partial fulfillment of the requirements
for the degree of Master of Science in Mechanical Engineering
in the Graduate College of the
University of Illinois at Chicago, 2017

Chicago, Illinois

Defense Committee:
Constantine M. Megaridis, Chair and Advisor
Jie Xu
Ranjan Ganguly, Jadavpur University, India

Copyright by

Uddalok Sen

2017

To my parents,
for the countless bed of nails they have walked on, carrying me on their shoulders.

ACKNOWLEDGMENTS

I believe that any meaningful experimental research cannot be conducted single-handedly, and the present study is no exception. This, however, poses the question as whom to thank for a certain work? Strictly speaking, this number in this case is quite large, and would call for a major relaxation on the page limit for the acknowledgements section. In light of such limitations, and also to keep the reader interested in the important stuff that follows, I will restrict this section to only thank the people that have influenced this work first hand.

This work would not have been possible if Prof. Constantine Megaridis had not allowed me to join his lab (MNFTL) in January 2016, at a time when things were not really working out for me. It has been almost two years since, and I have enjoyed every single moment I have spent in MNFTL. His constant support, dedication and commitment towards ethical scientific research, and attitude towards his students has constantly motivated, and still motivates, me to work at the high standards that MNFTL is associated with. At a time when my friends and peers at other labs complain as to how they dislike their life as a graduate student and the immense pressure that their advisors have put on them, I am truly grateful that Prof. Megaridis has always allowed me to work in my own time and caring about results rather than how much time I spend in the lab.

I would not even be associated with MNFTL if it was not for Prof. Ranjan Ganguly. He made my acquaintance with Prof. Megaridis, and I cannot thank him enough for the opportunities that he has always presented me with, and also for having the best intentions

ACKNOWLEDGMENTS (Continued)

in mind for me all the time. A fantastic mentor and a superb critic, my foray into academic research would not have been possible without him. To be frank, with him calling the plays, graduate school does not seem to be that difficult.

I would also like to take this opportunity to thank Prof. Jie Xu for being a part of my thesis defense committee. His insightful comments have made the present work much better than what it was during its infancy.

This work also would not have been possible if Dr. Souvick Chatterjee was not there assisting me everyday with my experiments, and I am immensely grateful for that. Quite the polar opposite of the bossy post doc, Dr. Chatterjee is, hands down, the best colleague one expects to have. Outside of work, he has been a great friend, and a helpful hand whenever I needed one in this foreign land. Whether it be about the experiments, the writing, or some non-academic personal issue, he has always been the first person that I have called up, and I am glad that none of those calls ever went to voicemail. It deeply saddens me that he would be leaving MNFTL in a few months, and its extremely selfish of me, but I wish he would have stayed to help me in the next leg of my academic pursuits. Nevertheless, I wish him all the very best for his future endeavors.

I am grateful to my fellow labmates Theodore Koukoravas and Jared Morrisette for providing invaluable help in acquiring the optical profilometer and scanning electron microscope data, respectively. Aritra also deserves mention in this regard for identifying some key references that the present work benefitted from. David Mecha at the College of Engineering Machine Shop assisted in sample fabrication, and I am thankful for that. I also thank the staff at the

ACKNOWLEDGMENTS (Continued)

Nanotechnology Core Facility for their support while using their equipment. I am also grateful to Kimberly-Clark Corporation for their generous financial support during the course of this study.

Finally, I would like to thank my parents for being who they are. There are not enough words in the English language to describe my feelings towards them, and if I am able to be even a tenth of the person they are, it would be a life well lived.

US

TABLE OF CONTENTS

<u>CHAPTER</u>	<u>PAGE</u>
1 INTRODUCTION	1
2 MATERIALS AND METHODS	9
3 RESULTS AND DISCUSSION	13
3.1 Liquid spreading	13
3.2 Dynamics of spreading	17
4 CONCLUSIONS AND FUTURE SCOPE	27
APPENDICES	30
Appendix A	31
Appendix B	33
Appendix C	35
Appendix D	37
CITED LITERATURE	38
VITA	46

LIST OF TABLES

<u>TABLE</u>		<u>PAGE</u>
I	PROPERTIES OF THE DIFFERENT WORKING FLUIDS USED IN THE PRESENT WORK (AT 25° C) (72; 73)	13

LIST OF FIGURES

<u>FIGURE</u>	<u>PAGE</u>
1 (a) Equilibrium contact angle of a sessile droplet and (b) wetting regimes for sessile drops	2
2 Origin of the driving force on a liquid droplet being transported along a wettability-confined wedge-shaped track. Reproduced from (12) with permission from The Royal Society of Chemistry	6
3 Schematic of the sample preparation procedure: (a) Al samples were first treated with a 4 M HCl solution for 5 minutes; (b) scanning electron micrograph of acid-etched sample; (c) acid-etched samples were passivated in boiling deionized water for 60 minutes; (d) scanning electron micrograph of etched-and-boiled sample; (e) the etched-and-boiled samples were then treated in an ethanolic solution of fluoro-alkyl silane (FAS) and kept undisturbed for 8-10 hours; (f) a CAD-based design was patterned onto the substrate by laser ablation; (g) top view of final sample containing the superhydrophobic and the superhydrophilic domains; (h) sessile water droplet on superhydrophobic domain (the scale bar denotes 1 mm)	10
4 Schematic of the experimental setup	11
5 Time lapse images of water spreading on a wettability-patterned wedge-shaped track: (a) instant of droplet touching the narrow end of the track ($t = 0.001$ s); (b) bulge volume stationary while hemiwicking front (HF) advances ($t = 0.010$ s); (c, d, e) both bulge and liquid front move together, with the advancing bulge (AB) gradually decreasing in height ($t = 0.020, 0.040, 0.080$ s); (f) bulge has disappeared and entire liquid volume moves as a rivulet ($t = 0.120$ s); (g) bulk liquid has become almost stationary and acts as a source for liquid spreading on superhydrophilic surface at a much slower rate ($t = 0.360$ s); (h) liquid front reaches the end of the track ($t = 1.200$ s)	16

LIST OF FIGURES (Continued)

<u>FIGURE</u>		<u>PAGE</u>
6	Liquid distribution on wedge-shaped track: (a1) Generic liquid volume side view when bulge exists; (a2) cross-section of liquid volume (at section A-A') when bulge exists, contact angle (θ) at wettability-contrast line greater than 90° ; (b1) generic liquid volume morphology when bulge has disappeared; (b2) cross-section of liquid volume (at section A-A') when bulge has disappeared, contact angle (θ) at wettability-contrast line smaller than 90°	17
7	Time lapse images of droplet of 50% aqueous solution of glycerol spreading on a wettability-patterned wedge-shaped track: (a) instant of droplet touching the narrow end of the track ($t = 0.001$ s); bulge volume stationary while hemiwicking front advances ($t = 0.060$ s); (c, d, e) both bulge and liquid front move together, with the bulge gradually decreasing in height ($t = 0.080, 0.180, 0.340$ s); (f) bulge has disappeared and entire liquid volume moves as a rivulet ($t = 0.520$ s); (g) bulk liquid has become almost stationary and acts as a source for liquid spreading on superhydrophilic surface at a much slower rate ($t = 1.100$ s); (h) liquid front still does not reach the end of the track at $t = 3.870$ s	18
8	Liquid front location (x) at different time instants (t); C_m indicates the mass fraction of glycerol in solution; shaded zones represent error limits corresponding to each color	19
9	Dimensionless front location (X) plotted against dimensionless time instant (T); three regimes marked as I, II, and III; inset (lower left) shows regime I plotted against the Washburn scale of droplet spreading; inset (upper right) shows regime III plotted against the density augmented-Tanner scale spreading. The dashed line in the lower left inset shows the straight line that the data points approximately follow. The location of the transition from one regime to the next has been determined by plotting X against T in the log-log scale, as shown in Figure 10 of the Appendix	22
10	Average dimensionless front location (X) plotted against dimensionless time instant (T) in log-log scale. The changes in slope demarcate the transition from one regime of spreading to the next	32
11	Dimensionless front location, X , plotted against dimensionless time, T , for a 0.01M aqueous solution of sodium dodecyl sulfate (SDS, $\gamma = 37$ mN/m) along with the average variation of X with T for water and the aqueous solutions of glycerol	34

LIST OF FIGURES (Continued)

<u>FIGURE</u>		<u>PAGE</u>
12	A representative image showing the change of pixel intensity (I) along the spreading liquid volume	36

SUMMARY

Spontaneous pumpless transport of liquid droplets on wettability-patterned tracks is important for a number of diverse applications such as rapid transport and mixing of fluid droplets, enhancing dropwise condensation on surfaces, and in the biomedical sector as well. Recent studies point to the fact that, on an open surface, a superhydrophilic diverging track laid on a superhydrophobic background results in pumpless transport of water from the narrow end to the wide end at unprecedented rates. However, the interplay between the driving capillary force and the resisting viscous force, which governs the spreading behavior of liquid droplets on such surfaces have so far not been characterized. Potential applications for transporting organic liquids and in point-of-care devices hence calls for understanding the spreading behavior of viscous droplets on such surfaces. An effort to do the same has been made in the present work by experimentally observing the spreading of liquid droplets of different viscosities and surface tensions on the aforementioned wettability-patterned diverging or wedge-shaped tracks. An universal relationship of the spreading behavior in terms of two dimensionless variables is obtained. The liquid spreading front was found to follow three distinct temporal scales, transitioning from a Washburn-type spreading to a much faster Laplace-pressure driven spreading, and finally to an extremely slow, density augmented-Tanner-type spreading.

CHAPTER 1

INTRODUCTION

Microfluidic systems are ubiquitous in the modern world, capable of performing a variety of practical tasks in applications where precise handling of liquid microvolumes is paramount. Such systems are characterized by their high surface area-to-volume ratio, which results in their ability to handle liquid microvolumes with a high level of accuracy and at a much reduced cost as compared to their macroscale counterparts. These advantages have made microfluidic devices immensely suitable for a range of applications, primarily in the medical, chemical, and biological sectors (1). The development of a vast number of techniques for fluid volume manipulation in microfluidic devices (2), such as capillary (3) and pressure-driven flows (4), electrokinetics (5), centrifugal (6), magnetic (7), and acoustic forces (8) has made handling and manipulating fluid microvolumes much easier. However, conventional 3D channel-based microfluidics have several practical problems such as non-specific interactions of the analyte/reagent with the walls of the channel, bubble clogging (9), and fouling by debris (10). These challenges are non-existent in microfluidic devices where the liquid is handled on an open surface instead of a closed channel, which in turn has led to the proliferation of open-surface microfluidic devices for a variety of applications (11). Apart from the mitigation of the aforementioned difficulties associated with closed-channel microfluidic systems, the 2D nature of open-surface microfluidics also results in a manifold reduction of the fabrication time. Moreover, there is no requirement of impervious solid walls for fluid confinement in open-surface microfluidics, resulting in its applicability over

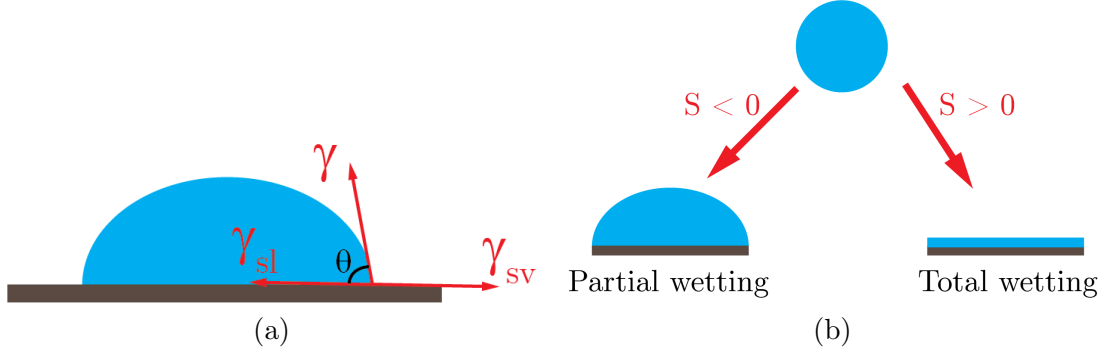


Figure 1. (a) Equilibrium contact angle of a sessile droplet and (b) wetting regimes for sessile drops

a diverse range of surfaces such as rigid and flexible substrates (12), porous materials (13), and even liquid-infused hybrid materials (14).

Open-surface microfluidics is essentially a subset of digital microfluidics (15), where instead of a continuous fluid stream, a single droplet is handled as the analyte for the microfluidic task. The characteristic length scale of the droplet in such devices is almost always less than the capillary length scale (16), which entails that forces generated due to the liquid surface tension, originating from spatial changes in the surface energy of the substrate or the droplet, can give rise to motion of the liquid volume. A surface is said to be hydrophobic if it repels water and hydrophilic if it attracts water. The most primitive test to check the affinity of a surface towards water is to deposit a droplet of water (having diameter less than the capillary length scale) on the substrate and measure the sessile or equilibrium contact angle (θ , as shown in Figure 1a). Hydrophobic surfaces have $\theta > 90^\circ$ while hydrophilic surfaces have $\theta < 90^\circ$. The prefix ‘super’ is applied to a hydrophobic surface if $\theta > 150^\circ$ and to a hydrophilic surface when

$\theta < 5^\circ$. The affinity of a liquid towards a substrate is essentially determined by the liquid-vapor (γ), solid-vapor (γ_{sv}), and solid-liquid (γ_{sl}) interfacial tensions. The balance of the interfacial forces at the contact line (Figure 1a) leads to the very well-known Young's equation (16):

$$\gamma \cos \theta = \gamma_{sv} - \gamma_{sl} \quad (1.1)$$

The contact angle, θ , is observed when the droplet is sessile or at rest. If the droplet starts to move in one direction, then the contact angles at its leading and trailing edges are usually different, and not equal to the sessile or equilibrium contact angle (16). In order to quantify whether a liquid droplet will spread on a solid surface or not, a metric known as the spreading parameter (S) is often used. The spreading parameter can be expressed as:

$$S = \gamma_{sv} - (\gamma_{sl} + \gamma) \quad (1.2)$$

Physically, the spreading parameter represents the difference in the surface energy (per unit area) of the substrate when it is dry and wet. A positive value of the spreading parameter ($S > 0$, Figure 1(b)) refers to a partial wetting scenario, while for a negative value ($S < 0$, Figure 1(b)), the liquid will completely wet the surface. Hence, for $S > 0$, a spherical bead-shaped droplet is formed, while a nanoscopic film of the liquid rests on the substrate when $S < 0$. When $S > 0$, for a homogeneous surface, a droplet of liquid will spread uniformly in all radial directions until it reaches the equilibrium configuration. The different modes of

droplet spreading on a homogeneous substrate due to the equilibrium of various forces have been extensively reviewed by Bonn et al. (17).

Water droplets can be confined by the energy barrier at the superhydrophobic-superhydrophilic contrast line (18), and the maximum volume of water that can be confined is governed by the sessile-droplet contact angles at the superhydrophobic and superhydrophilic domains (19). Several facile techniques for creation of surfaces with extreme wettability contrast have been developed recently (20), which in turn has led to the impetus in scientific research on confining droplets on the surface of a chip or a substrate using hydrophilic and hydrophobic domains (21; 22; 23; 24; 25). Applications as diverse as atmospheric water collection (26) and surface-enhanced Raman spectroscopy (27; 28; 29) have been developed with such techniques of wettability patterning. Manipulation of liquids using patterned wettability can be employed not only to solid substrates, but on paper (30) and fabrics (31) as well.

In general, a source of actuation, such as gravity (24) or the Laplace pressure difference between two droplets of different diameters (25), is always required for transporting droplets on surface-tension confined tracks. However, a plethora of methods (32) exist for ‘pumpless’ manipulation of droplets on such wettability patterned tracks by dynamically changing the surface energy of the droplet. The tendency of a liquid droplet to attain a morphology on the substrate in order to minimize the overall energy of the system can be harnessed to achieve spontaneous, directional movement of the droplet on an aptly designed substrate. The most popular technique to achieve this has been physical texturing or micropatterning of the substrate (33; 34; 35; 36), where a spatial variation of the surface roughness parameter of the

substrate leads to a spatial heterogeneity of the affinity of the substrate towards the droplet. However, ‘pumpless’ transport of liquid droplets can also be achieved by a surface energy gradient due to chemical modification of the substrate (37) or the droplet (38; 39), differential heating of the substrate in the presence of a hydrophilicity gradient (40; 41), chemically-assisted thermocapillary migration (42), photo-irradiated liquid manipulation (43) and by harnessing the Leidenfrost effect (44; 45). An extensive review of wettability gradients created by external agents can be found in (46). Unidirectional ‘pumpless’ transport of liquids on porous substrates can be achieved by utilizing the wicking phenomenon, where a droplet volume is transported from one point on the substrate to the other by gradually filling the microcapillaries present in the porous substrate. Wicking-based transport is most commonly observed in the case of paper-based microfluidics, which has shown great promise in biodiagnostics (47) and also oil recovery (48). Recent review articles (49; 50) have extensively studied the growth and future of paper-based microfluidic devices. Apart from paper substrates, wicking-based microfluidics have been employed in textile substrates (51; 52) as well.

A novel liquid manipulation technique was recently introduced by Ghosh et al. (12) where self-propulsion of a water droplet was observed from the narrow end to the wide end of a diverging or wedge-shaped superhydrophilic track laid on a superhydrophobic substrate. The driving mechanism is shown as a schematic in Figure 2. The diverging nature of the track resulted in a constantly changing droplet footprint area. This further leads to an axial variation of the curvature of the liquid meniscus, resulting in a Laplace-pressure generated force along the axial direction of the track. This force will always push the droplet from a smaller wetted

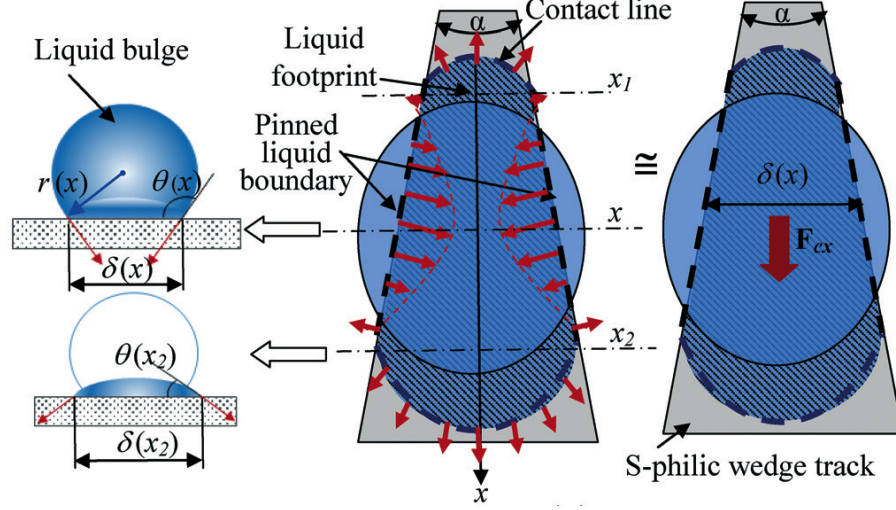


Figure 2. Origin of the driving force on a liquid droplet being transported along a wettability-confined wedge-shaped track. Reproduced from (12) with permission from The Royal Society of Chemistry

footprint to a larger one as it reduces the overall energy of the system. Further details on the motion of droplets on such wettability-patterned tracks are mentioned in Chapter 3 of the present work. Apart from horizontal substrates, such wettability-patterned wedge-shaped tracks have also been shown to transport water droplets up an incline against gravity (12; 53; 54). This particular geometrical configuration bears resemblance to a two-dimensional analog of spontaneous droplet transport on conical wires that has been studied previously (55). The wettability contrast in such configurations can be created by functionalizing a single substrate (12) or by leveraging the difference in water contact angles of two dissimilar materials (56). Literature bears testimony to the fact that such wettability-patterned wedge-shaped tracks are immensely useful for a diverse array of applications such as liquid manipulation using multiple

triangular patches (57), spontaneous mixing of aqueous droplets containing different reagents (58), and enhancing heat transfer performance in dropwise condensation studies (59; 60; 61) and for electronics cooling (62).

The aforementioned wettability-confined wedge tracks are not only limited to transporting aqueous droplets – as evident from recent studies that have used such tracks for transporting organic liquid droplets under water (63) and ferrofluids (64). Surface tension and viscosity of the fluids being transported are the two most important properties that determine the transport characteristics. The difference in the liquid contact angles between the lyophilic (surface on which a liquid spreads spontaneously) and lyophobic (surface on which a liquid does not spread spontaneously) domains is the principal driving force for the liquid droplet. Hence the surface tension of the fluid affects the transport in a way that a higher wettability contrast results in a larger magnitude of the driving force. However, the influence of viscosity on dynamics of the liquid transport cannot be guessed *a priori*, thus calling for rigorous experimental characterization. Although a plethora of studies exists on dynamic spreading of liquids on homogeneous unconfined substrates (65; 66; 67; 17), no such literature is available on the spreading dynamics of droplets on wedge-shaped wettability-confined tracks. Moreover, microfluidic devices are frequently used in the biomedical sector (68) as point-of-care devices, where the working fluid is seldom aqueous. Thus the need to understand the role of viscosity in pumpless transport of liquid droplets on wettability-patterned wedge-shaped tracks cannot be overemphasized, and an effort to study the same has been made in the present work.

The objectives of the present work can be briefly summarized as:

- Develop wettability-patterned substrates for pumpless liquid transport on metal substrates (Al)
- Study the effect of fluid viscosity on the transport rate of droplets on such substrates
- Develop a scaling analysis to characterize the relative importance of the viscous drag and the driving capillary forces

The organization of the thesis is as follows: the experimental methods and the materials used are described in Chapter 2. Chapter 3 details the experimental results. The morphological evolution of a droplet placed on an aforementioned wettability-confined diverging track is presented first. Subsequently, the development of the scaling arguments leading to the description of universal behavior is highlighted. Finally, Chapter 4 concludes the thesis by summarizing the key results of the work and outlining its future scope.

CHAPTER 2

MATERIALS AND METHODS

The superhydrophobic and superhydrophilic domains were produced by a facile and scalable approach on rectangular aluminum samples 50 mm long and 25 mm wide (mirror-finish 601 aluminum sheets, 2 mm thick, McMaster-Carr). The sample fabrication procedure was identical to the one reported by Koukoravas et al. (62), where the samples were first treated with a 4 M HCl solution (ACS Reagent 37%, Sigma-Aldrich) for 5 minutes (Figure 3a) before passivation in boiling deionized water for 60 minutes (Figure 3c). This results in the formation of micro-nano structures on the aluminum surface, with the boiling step also resulting in the formation of a thin layer of aluminum oxide hydroxide (Al(O)OH), commonly known as böhmite (69), on the surface of the substrate. Taking cue from existing literature (70; 71), the superhydrophilic etched-and-boiled aluminum samples were immersed in an 1% (by weight) ethanolic (200 proof, Decon Labs) solution of 1H, 1H, 2H, 2H-Perfluorodecyltriethoxysilane (97%, Sigma-Aldrich, abbreviated as FAS for fluoro-alkyl silane) for 8-10 hours (Figure 3e). A monolayer of FAS thus formed on the roughened Al samples, imparting superhydrophobicity.

A ‘zoomed-in’ view of the micro-nano structures formed on the sample can be obtained through scanning electron micrographs (obtained using the imaging module of a Raith 100 eLINE Electron Beam Lithography System), as shown in Figure 3b and Figure 3d. The acid etching step results in the formation of microscale terraces and caverns (Figure 3b), which are subsequently covered by nanoscale böhmite needles (Figure 3d) upon passivation. Such

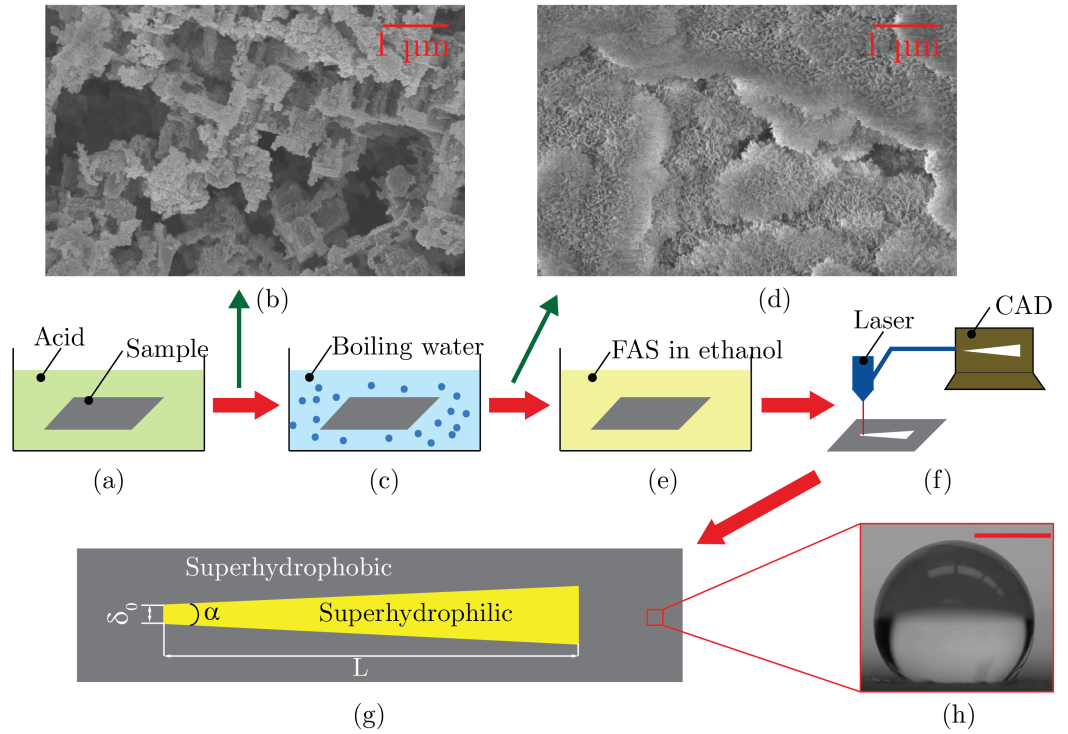


Figure 3. Schematic of the sample preparation procedure: (a) Al samples were first treated with a 4 M HCl solution for 5 minutes; (b) scanning electron micrograph of acid-etched sample; (c) acid-etched samples were passivated in boiling deionized water for 60 minutes; (d) scanning electron micrograph of etched-and-boiled sample; (e) the etched-and-boiled samples were then treated in an ethanolic solution of fluoro-alkyl silane (FAS) and kept undisturbed for 8-10 hours; (f) a CAD-based design was patterned onto the substrate by laser ablation; (g) top view of final sample containing the superhydrophobic and the superhydrophilic domains; (h) sessile water droplet on superhydrophobic domain (the scale bar denotes 1 mm)

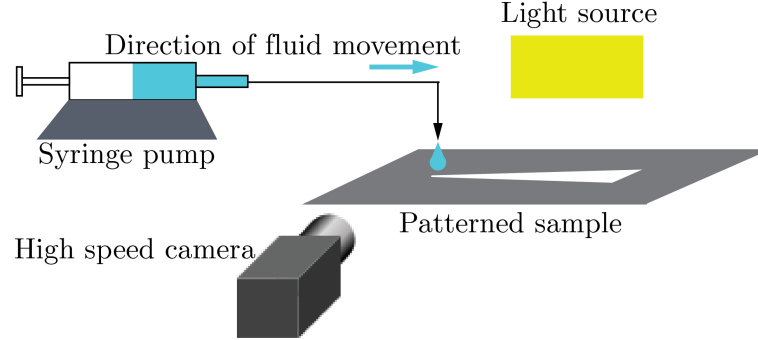


Figure 4. Schematic of the experimental setup

surface features where nanoscale structures are formed on top of microscale structures are known as hierarchical structures, and are essential for superhydrophilic and superhydrophobic behavior. The average roughness features of the surface were found to be of the order of $25\ \mu\text{m}$ (measured using a Wyko NT3300 Optical Profilometer). The roughness features when covered by a monolayer of FAS reduces the surface energy of the exposed area. An in-house goniometer was used to measure the sessile contact angle of the superhydrophobic domain (Figure 3h), which was found to be $152 \pm 1^\circ$. On the other hand, a droplet deposited on the superhydrophilic domain spread instantly with a contact angle less than 5° .

A laser marking system (EMS400, TYKMA ElectroX) fitted with a Yb laser (20% power, 20 kHz frequency, 200 mm/s traverse speed, Scorpion Rapide, TYKMA ElectroX), along with a computer-aided design (CAD) file as vector image input, was used to selectively ablate the FAS coating on the Al samples (Figure 4). The underlying superhydrophilic domain was exposed via the ablation procedure, while the unharmed regions continued to exhibit superhydrophobicity.

A schematic top view of the finished sample, as obtained from the aforementioned procedure, is shown in Figure 3g, along with the salient dimensions. For the present work, a track of length (L) of 30 mm, narrow end width (δ_0) of 500 μm , and divergence angle (α) of 4° was chosen for experimental observations.

Glycerol-deionized water solutions (99+%, Alfa Aesar), having mass fractions of glycerol varying from 0.1-0.5, were used as the working fluid. The experimental setup is shown as a schematic in Figure 4. A syringe infusion pump (PHD Ultra, Harvard Apparatus) was used to dispense a single drop (mass ~ 4.5 mg) through a 100 μm inner diameter needle (32GA GP, Nordson EFD) onto the superhydrophilic tracks. The droplet was dispensed in a way that there were no inertial effects, and while dispensing did not touch the needle and the substrate at the same time. In other words, the droplet detached from the nozzle before its bottom came into contact with the substrate. A high-speed camera (Phantom Miro 310, Vision Research AMETEK) mounted with a prime lens (Nikkor 50 mm, Nikon) was used to capture high speed videos, at 1000 fps (frames-per-second), of the fluid flow on the superhydrophilic tracks. A portable halogen light source (L860, 250 W, Workforce) was used for illuminating the sample through a rectangular diffuser sheet (Lumen XT LT LW7, Makrolon). The image processing feature of the commercial software MATLAB was used to analyze the sequential high speed images obtained from the high speed videography, where the instantaneous position of the liquid front was demarcated by a sharp jump in the pixel intensity.

CHAPTER 3

RESULTS AND DISCUSSION

Aqueous solutions of glycerol (having glycerol mass fractions, C_m , ranging from 0.1-0.5), and water were used as working fluids in the present work. For each of the working fluids, a droplet of ~ 4.5 mg was deposited at the narrow-end of a wedge-shaped track of length 30 mm, initial width 500 μm , and divergence angle of 4° . The experiments were performed at 25°C , and the salient properties of the fluids at that condition are presented in Table I (72; 73).

3.1 Liquid spreading

Figure 5 presents time lapse images of different stages of a water droplet spreading on a wedge-shaped wettability-patterned track. A spherical droplet, when dispensed on the narrow end (left) of the track without any initial velocity (Figure 5a), remains confined on the two

TABLE I

PROPERTIES OF THE DIFFERENT WORKING FLUIDS USED IN THE PRESENT
WORK (AT 25°C) (72; 73)

Glycerol mass fraction, C_m	Density (kg/m^3)	Surface Tension (mN/m)	Viscosity (mPa.s)
0 (water)	997.0	72.45	0.903
0.1	1021.3	71.83	0.928
0.2	1045.5	71.20	1.555
0.3	1072.3	70.28	2.185
0.4	1099.0	69.35	3.220
0.5	1125.3	68.63	5.105

transverse sides of the track by the wettability-contrast line, and can spread only in the length-wise direction to the wider end of the track (right). The bulk of the liquid volume is initially at rest, with a liquid front advancing as a film along the track (as marked in Figure 5b). The high mass of the bulge keeps it stationary, while the roughness features of the superhydrophilic domain prompts the liquid film to advance through it via hemiwicking (74). The liquid bulge starts to move after some time (Figure 5c), gradually decreasing in height as it spreads (Figure 5d), and ultimately catches up with the liquid front (Figure 5e). Soon after, the liquid bulge disappears and the entire spreading liquid volume resembles a rivulet (Figure 5f). The contact angle subtended by the liquid volume along the wettability-contrast line decreases as the droplet spreads, its value at any given instant staying between the respective sessile droplet contact angles of the superhydrophobic and superhydrophilic domains. The cross-section of the spreading liquid volume transitions from the morphology shown in Figure 6a2 (corresponding to section A-A' of Figure 6a1) to the one in Figure 6b2, with the contact angle (θ) at the wettability-contrast line changing from obtuse to acute as the liquid spreads. For rectangular channels, Brinkmann and Lipowsky (75) had pointed out that a spreading droplet forms a liquid bulge (which is confined in the transverse and elongated in the axial directions) when the local contact angle along the wettability-contrast line is greater than 90° , the morphology being reversible with the bulge disappearing when the same angle is less than 90° . A similar argument can be made for these aforementioned wedge-shaped tracks, where the liquid indeed forms a moving bulge in the initial phase of spreading. However, a detailed analysis is required to identify the critical local contact angle for bulge formation – a study which was beyond the

scope of the present work. The liquid droplet spreads as the fluid volume tries to minimize its surface energy. The leading edge of the spreading liquid bulge has a longer contact line than the trailing edge (leading and trailing edges marked as LE and TE, respectively in Figure 5d), which leads to an unbalanced capillary force (marked as F_{cap} in Figure 5) driving the liquid from the narrow end to the wide end of the track. A forward-direction capillary force exists as long as a distinct liquid bulge exists, and the axial component of the net capillary force results in motion of the liquid volume. The bulge height decreases as the liquid spreads further; the bulge ultimately disappearing after some finite spread distance. When the bulge has disappeared, a reversal of the direction of the net capillary force occurs, resulting in a retardation of the liquid volume. The forward motion of the liquid volume is also hindered by the presence of viscous drag, which results in an increasingly slower motion. Finally, an instant can be identified beyond which the bulk liquid spreads extremely slowly, almost coming to a halt (Figure 5g). However, the local curvature of the stationary liquid volume is sufficient for driving a thin film that creeps sluggishly towards the wider end of the track (Figure 5h).

Time lapse images of the spreading of a droplet of an aqueous solution of 50% (by mass) glycerol on an identical track are shown in Figure 7. The spreading features are exactly identical to that of a water droplet (Figure 5). However, the time instants at which each mode is observed are drastically different, clearly indicating that the glycerol solution, expectedly, spreads much slower than water. The approximately 5 times higher viscosity of the glycerol solution (as shown in Table I) is responsible for this behavior. The viscous force, by its nature, opposes fluid motion, hence acting against the capillary force. This results in a much weaker net driving

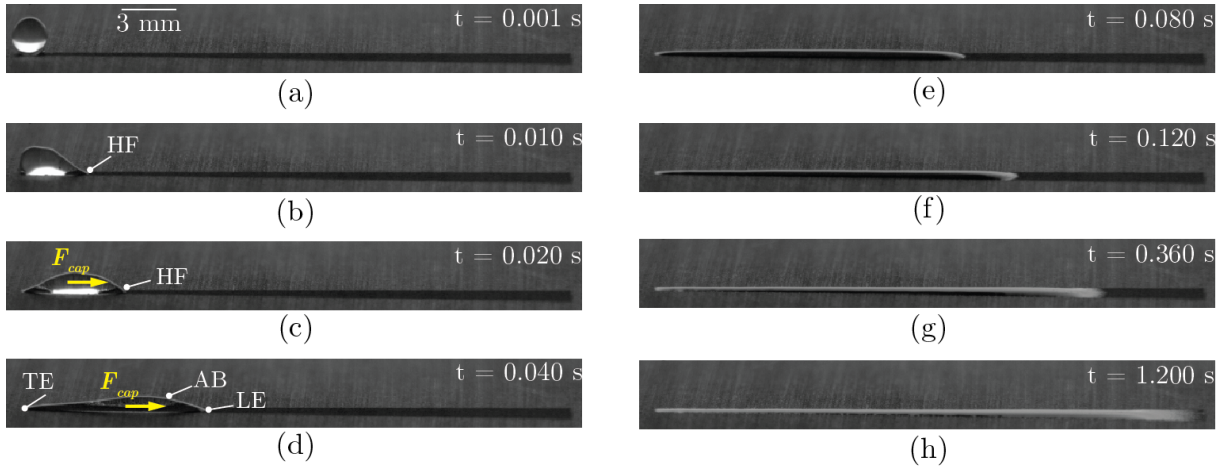


Figure 5. Time lapse images of water spreading on a wettability-patterned wedge-shaped track: (a) instant of droplet touching the narrow end of the track ($t = 0.001$ s); (b) bulge volume stationary while hemiwicking front (HF) advances ($t = 0.010$ s); (c, d, e) both bulge and liquid front move together, with the advancing bulge (AB) gradually decreasing in height ($t = 0.020, 0.040, 0.080$ s); (f) bulge has disappeared and entire liquid volume moves as a rivulet ($t = 0.120$ s); (g) bulk liquid has become almost stationary and acts as a source for liquid spreading on superhydrophilic surface at a much slower rate ($t = 0.360$ s); (h) liquid front reaches the end of the track ($t = 1.200$ s)

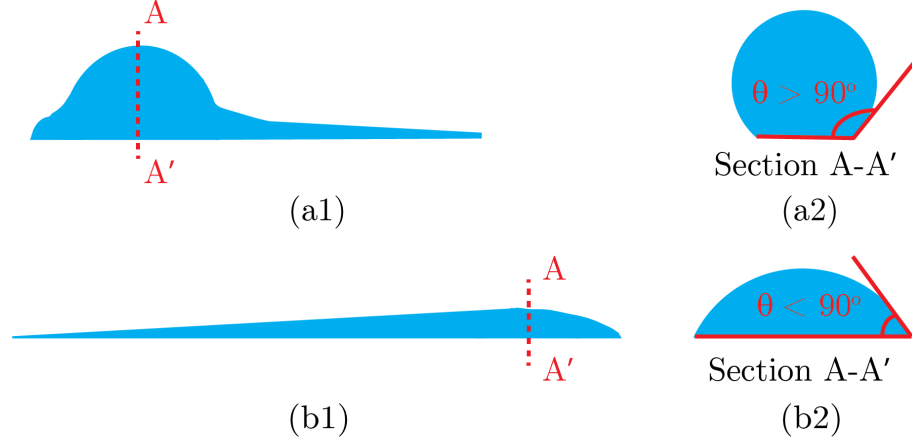


Figure 6. Liquid distribution on wedge-shaped track: (a1) Generic liquid volume side view when bulge exists; (a2) cross-section of liquid volume (at section A-A') when bulge exists, contact angle (θ) at wettability-contrast line greater than 90° ; (b1) generic liquid volume morphology when bulge has disappeared; (b2) cross-section of liquid volume (at section A-A') when bulge has disappeared, contact angle (θ) at wettability-contrast line smaller than 90°

force for the liquid volume. The capillary force also decreases with decreasing surface tension (12), but as Table I shows, the surface tension values of the all the working fluids tested in the present study are similar with little variation. Hence, there is minimal reduction of the capillary force due to surface-tension changes. A lower net driving force results in a more sluggish spreading of the droplet, which for the case shown in Figure 7, does not even reach the end of the track at the end of the recording window (Figure 7h).

3.2 Dynamics of spreading

A quantitative variation of the liquid front position (x) with time (t) is obtained from image processing of the high-speed videos, which has been subsequently plotted in Figure 8 for different mass fractions (C_m) of glycerol in solution. All the curves show similar trend, with the

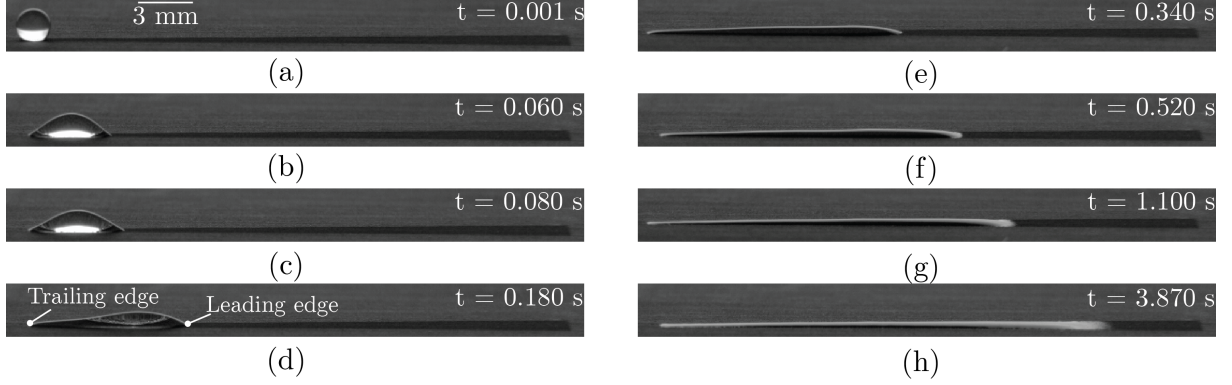


Figure 7. Time lapse images of droplet of 50% aqueous solution of glycerol spreading on a wettability-patterned wedge-shaped track: (a) instant of droplet touching the narrow end of the track ($t = 0.001$ s); bulge volume stationary while hemiwicking front advances ($t = 0.060$ s); (c, d, e) both bulge and liquid front move together, with the bulge gradually decreasing in height ($t = 0.080, 0.180, 0.340$ s); (f) bulge has disappeared and entire liquid volume moves as a rivulet ($t = 0.520$ s); (g) bulk liquid has become almost stationary and acts as a source for liquid spreading on superhydrophilic surface at a much slower rate ($t = 1.100$ s); (h) liquid front still does not reach the end of the track at $t = 3.870$ s

front position initially increasing rapidly in time, but then progressing rather sluggishly. The trend observed with increasing glycerol mass fractions is also unsurprising – a water droplet ($C_m = 0$) having the lowest viscosity among all the fluids reaches the end of the track in 1.2 s, while a droplet having $C_m = 0.5$ (which has the highest viscosity among the fluids tested) does not reach the end of the track even after 3.87 s. The similarity in the trends observed in Figure 8 suggests that a proper non-dimensionalization of the relevant spreading parameters may reveal a universal curve highlighting the underlying physics of the problem.

Two dimensionless quantities were introduced – a dimensionless liquid front location, X , defined as x/L , and a dimensionless time, T , defined as $(\gamma t/\mu L)$, where γ and μ respectively

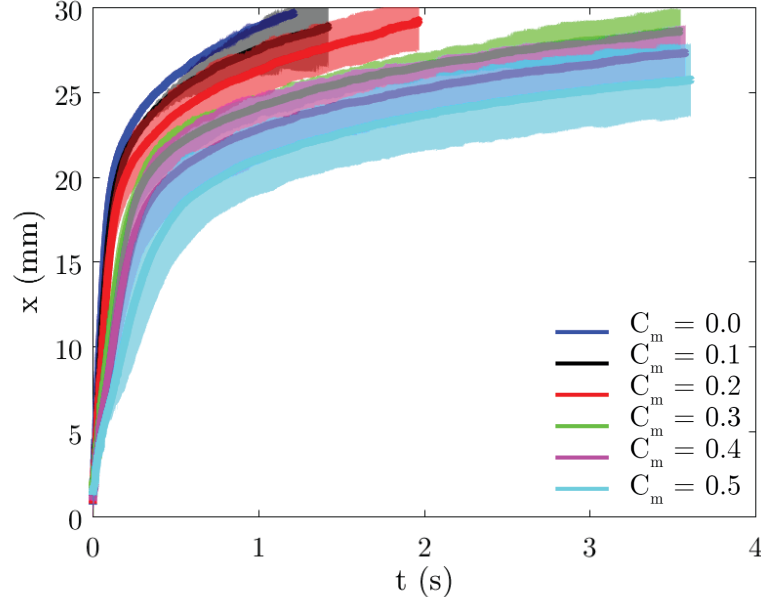


Figure 8. Liquid front location (x) at different time instants (t); C_m indicates the mass fraction of glycerol in solution; shaded zones represent error limits corresponding to each color

denote the surface tension and the viscosity of the fluid. The variation of X with T , as observed in the present work for all the working fluids considered, is shown in Figure 9. The non-dimensional curves for all the fluids are found to collapse upon each other, and three distinct regimes of spreading are observed, henceforth denoted as I, II, and III. Regime I corresponds to the time period when the liquid bulge has not yet picked up a discernible velocity and only a thin film advances from it (Figure 5b and Figure 7b); hemiwicking is responsible for the spreading of the liquid through the textured superhydrophilic track. Two forces primarily influence the spreading in this regime – the capillary-pull through the crevices (which may be assumed analogous to a bundle of hydrophilic microchannels (24)) on the rough track, and the viscous

force opposing the flow. For spreading of viscous droplets on unconfined substrates, researchers (76; 77) have shown that an early spreading regime exists where the spreading distance varies as $t^{1/2}$, the scaling being identical to the Washburn spreading law (78). The Washburn spreading law is commonly observed in wicking-based devices (79). Schutzius et al. (24) obtained the same scaling relationship for uni-directional droplet spreading on rectangular surface tension confined tracks. The variation of X with $T^{1/2}$ is shown in the lower left inset of Figure 9. The data points for all the fluids follow, approximately, a straight line (represented by the dashed line). After being dispensed from the nozzle, the droplet undergoes oscillations as it tries to simultaneously adjust its shape as well as spread along the track – these coupled phenomena lead to the observed deviations of some of the data points from straight line behavior. If the spreading distance, x , is larger (by more than two orders of magnitude in the present work) than the average diameter of the roughness structures of the surface, d_{pore} , a Poiseuille flow approximation of the velocity of the liquid front, u , leads to

$$u \sim \frac{d_{pore}^2}{\mu} \frac{\Delta p}{x} \quad (3.1)$$

where Δp is the capillary pressure difference driving the flow. The liquid meniscus has a mean curvature $\sim 1/d_{pore}$ at the crevices of the surface microstructure, leading to

$$\Delta p \sim \frac{\gamma}{d_{pore}} \quad (3.2)$$

Rewriting u as x/t , the expression of u in Equation 3.1 becomes

$$\frac{x^2}{t} \sim \frac{\gamma}{\mu} d_{pore} \quad (3.3)$$

The approximate straight line behavior of the datapoints in the lower left inset of Figure 9 confirms the Washburn behavior, indicating that the liquid front spreading is primarily governed by the hemiwicking on the rough superhydrophilic surface. Regime I extends from the moment the droplet touches the superhydrophilic track to the point where the liquid bulge overcomes its inertia and starts to move.

A balance between the unbalanced capillary force (due to the shape of the liquid meniscus of the traveling liquid bulge) propelling the liquid bulge forward and the resistive viscous force gives rise to the second regime of spreading. The axial force acting on the liquid bulge is estimated as

$$F_{cap} \sim \frac{dp}{dx} A_{cs} x \quad (3.4)$$

with dp/dx denoting the axial variation of the Laplace pressure and A_{cs} the cross-sectional area of the liquid upon which the Laplace pressure acts. Taking cue from (12), the pressure gradient can be expressed as

$$\frac{dp}{dx} \sim 2\gamma \sin \theta_{avg} \frac{1}{\delta^2} \alpha \quad (3.5)$$

where θ_{avg} is the average contact angle along the wettability-contrast line over the length of the bulge and δ denotes the local track width. The spreading liquid volume causes θ_{avg} to gradually

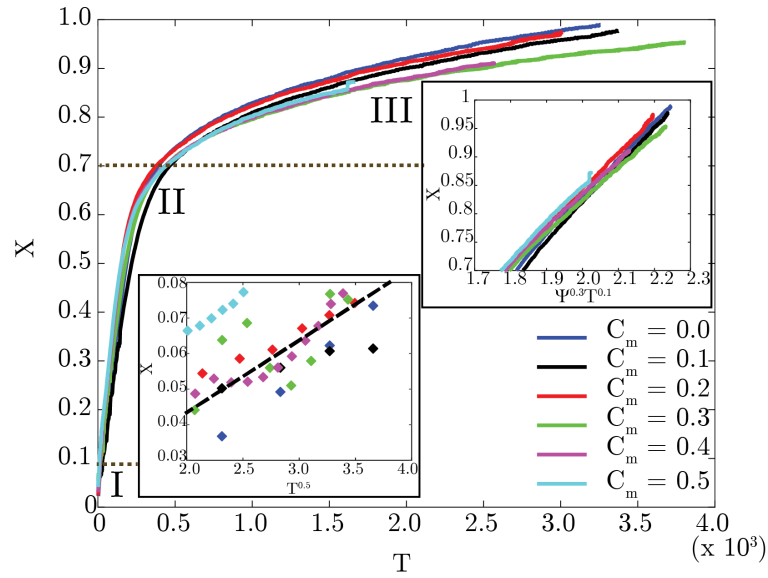


Figure 9. Dimensionless front location (X) plotted against dimensionless time instant (T); three regimes marked as I, II, and III; inset (lower left) shows regime I plotted against the Washburn scale of droplet spreading; inset (upper right) shows regime III plotted against the density augmented-Tanner scale spreading. The dashed line in the lower left inset shows the straight line that the data points approximately follow. The location of the transition from one regime to the next has been determined by plotting X against T in the log-log scale, as shown in Figure 10 of the Appendix

change from an obtuse to an acute angle, which further results in $\sin\theta_{avg}$ to change sign over the course of this spreading. Moreover, a diverging track means that δ increases with increasing axial distance, resulting in a gradual decrease of the pressure gradient. These two effects result in a decreasing net driving force of the liquid bulge. The cross-section of the liquid bulge can be assumed to be a sector of circle; thus $A_{cs} \sim \delta^2$. Therefore, for a given α , $F_{cap} \sim \gamma x$. The viscous resistance, on the other hand, is primarily experienced near the base of the liquid bulge where it is in contact with the solid substrate, and can be approximated as

$$F_{visc} \sim \mu \frac{u}{h} A_{base} \quad (3.6)$$

with u being the linear velocity of the liquid volume, h the height of the liquid bulge, and A_{base} representing the basal (footprint) area of the bulge volume. As previously mentioned, the bulge cross-section is considered to be the sector of a circle, which leads to $h \sim \delta$. The bulge volume is also assumed to have a trapezoidal footprint due to the diverging nature of the track, resulting in $A_{base} \sim \frac{1}{2}x\delta$. Therefore, the expression for the viscous force can be rewritten as

$$F_{visc} \sim \mu \frac{u}{h} x\delta \sim \mu \frac{x^2}{t} \quad (3.7)$$

A balance between F_{cap} and F_{visc} yields

$$x \sim \frac{\gamma}{\mu} t \quad (3.8)$$

which is a linear relationship between the front position and time. The experimental data (Figure 9) also shows the same linear scaling ($X \sim T$); which has been termed as Regime II. Regime II starts when the liquid bulge first starts to move and terminates as the bulge disappears and the bulk liquid becomes almost stationary.

Regime III commences with the bulk liquid volume coming nearly to rest and a thin liquid film creeping on the superhydrophilic substrate (Figure 5g and Figure 7g). This regime is primarily governed by the energy dissipation during viscous spreading, which has been classically attributed to three components (65) – viscous dissipation in the bulk of the droplet, dissipation at the contact line (80), and dissipation at the spreading precursor film (16). As a liquid droplet spreads, a ‘rolling motion’, similar to a caterpillar track, is observed on its surface, resulting in the viscous dissipation in the bulk droplet. This rolling motion results in packets of fluid from the free surface of the liquid volume to eventually end up at the vicinity of the solid substrate. Dissipation-governed spreading on unbounded substrates follows the well-known Tanner’s law (81), where the spreading radius scales as $t^{1/10}$. The lubrication approximation for such a flow results in an expression for the liquid front velocity (assuming Poiseuille flow) given by

$$u \sim \frac{h^2}{\mu} \frac{\Delta p}{x} \quad (3.9)$$

where h denotes the height of the spreading liquid volume. When $h \ll x$, the mean curvature of the spreading liquid front is $\sim h/x^2$ (82), and the pressure drop is given by

$$\Delta p \sim \gamma \frac{h}{x^2} \quad (3.10)$$

Hence, the spreading velocity can be rewritten as

$$u \sim \frac{x}{t} \sim \frac{\gamma}{\mu} \frac{h^3}{x^3} \quad (3.11)$$

However, h is not constant in Regime III, but varies with x . Instead, the spreading volume, Ω , is constant. The diverging nature of the track allows the spreading liquid volume to be considered a part of a trapezoidal prism, and volume conservation yields

$$\Omega \sim hx\delta \quad (3.12)$$

When α is small, $\delta \sim \alpha x$, leading to $\Omega \sim \alpha hx^2$. This further results in

$$h \sim \frac{\Omega}{\alpha x^2} \quad (3.13)$$

The pendant droplet size changes with fluid properties, which means that Ω is not constant for runs with different fluids. The quantity of dispensed droplet is, in essence, governed by a balance between gravity (shedding the droplet) and surface tension (restraining the droplet at

the needle tip) (83; 84). Hence, the effect of density variation on the dispensed liquid volume can be accounted for by

$$\Omega \sim \Omega_0 \frac{\rho_0}{\rho} \quad (3.14)$$

where the subscript ‘0’ corresponds to water. The effect of surface tension is ignored in Equation 3.14, since it does not change appreciably for the fluid samples used (Table I) as compared to the density. Hence,

$$\frac{x}{t} \sim \frac{\gamma}{\mu} \frac{1}{x^3} \Omega_0^3 \left(\frac{\rho_0^3}{\rho^3} \right) \frac{1}{\alpha^3 x^6} \quad (3.15)$$

$$\sim \frac{\gamma}{\mu} \frac{\Omega_0^3}{\alpha^3} \Psi^3 \frac{1}{x^9} \quad (3.16)$$

with Ψ denoting the ratio of ρ_0 and ρ , ρ being the density of the working fluid and ρ_0 being that of water. Hence, the scaling relationship for spreading in Regime III can be expressed as

$$x \sim \Psi^{3/10} \left(\frac{\gamma}{\mu} \right)^{1/10} t^{1/10} \quad (3.17)$$

This scaling relationship closely resembles the Tanner spreading law (81), with a weak density dependence augmented to that. The X against $\Psi^{3/10} T^{1/10}$ plot obtained from the experiments is shown in the upper right inset of Figure 9. The curves are observed to overlap on each other, and also follow a straight line. Hence, it is conclusive that the spreading front in Regime III adheres to the $X \sim \Psi^{3/10} T^{1/10}$ scaling law – which can be called a density-augmented Tanner-spreading law.

CHAPTER 4

CONCLUSIONS AND FUTURE SCOPE

The present work is a first-hand characterization of directional liquid spreading on diverging, wettability-confined tracks, highlighting the difference between classical spreading (on unconfined substrates or parallel tracks) and the pumpless rapid transport observed in wettability-patterned, diverging tracks. The droplet spreading behavior on a superhydrophilic wettability-confined, wedge-shaped track laid on a superhydrophobic background was studied. Water and aqueous solutions of glycerol, having mass fractions ranging from 0.1 through 0.5, were used as the working fluids to mimic a range of bio-fluids. High speed images revealed similar droplet spreading morphologies for the range of viscosities tested, the major difference being that the time taken by the liquid front to reach a particular axial location on the superhydrophilic track increases with increasing viscosity. Initially the droplet remains almost stationary in the form of a liquid bulge, having a thin precursor film of liquid hemiwicking through the roughness structures of the superhydrophilic track. In time, both the liquid front and the bulge move, with the bulge gradually decreasing in height as it spread. After some time, no discernible bulge volume can be observed, with the entire liquid volume spreading as a slender rivulet. The final stage of this spreading is when the bulk liquid volume becomes stationary, and a thin liquid front creeps across the rest of the superhydrophilic track.

The experimentally obtained dimensional liquid front position plotted against dimensional time accurately represents the spreading speeds and spreading morphologies. As expected,

the fluid with the lowest viscosity spreads the fastest, while the one with the highest viscosity spreads the slowest. All the other intermediate fluids have spreading characteristics between these two limits, and in ascending order of viscosity.

Introduction of a suitable dimensionless front position and a dimensionless time results in all the curves to collapse upon each other, suggesting universal behavior. Three regimes of spreading are identified, which correlate well with the changing liquid morphologies. In the first regime, the directional transport resembles the early-stage spreading of unconfined viscous droplets through hemiwicking, and the spreading front follows the Washburn scale ($X \sim T^{1/2}$). A balance between the net capillary force driving the liquid bulge and the resistive force results in the second regime of spreading, which is characterized by a linear scaling relationship ($X \sim T$). The third regime is contact line dissipation dominated, and a density-augmented Tanner’s law ($X \sim \Psi^{3/10} T^{1/10}$) is found to be the prevailing scaling relationship. It should be pointed out that such multiscale spreading of liquid droplets has been observed by other researchers (82; 76; 77) as well, but for unconfined homogeneous substrates. This is the first work that identifies multiple regimes of spreading of a droplet on a wettability-confined, diverging track.

The present study satisfactorily describes the directional spreading behavior of a viscous liquid droplet on wettability-patterned diverging or wedge-shaped tracks, highlighting the universal scaling of the spreading liquid front with time. Such tracks have potential applications in point-of-care devices, liquid mixing, and transport of oils and organic solvents – applications involving non-aqueous fluids having a diverse range of fluid properties. Such applications call

for the knowledge of how far and how fast a given fluid will spread on a particular geometry, hence facilitating design decisions and performance improvement of the device.

The present work highlights the first steps towards identifying the transport characteristics of complex fluids on wettability-confined, diverging tracks. Aqueous solutions of glycerol, which are used in the present work as the working fluid, exhibit Newtonian behavior, while almost all bio-fluids are non-Newtonian. Hence, a logical future step in this work would be to characterize the transport of non-Newtonian fluids on the same tracks. Moreover, the transport of the liquid in Regime II is governed by the magnitude of the wettability contrast between the hydrophobic and hydrophilic domains, and the effect of that can be investigated in a subsequent study. Furthermore, one can also use this design for point-of-care and point-of-injury diagnostic devices. One such application can be modifying existing wound dressings and coupling them with sensing and diagnostic modules where the liquid transport mechanism would be these tracks. Wound dressings are made from porous materials – which means that the transport of liquids on these diverging tracks laid out on porous substrates has to be characterized as well. Finally, the speed at which a blood sample spreads across the aforementioned tracks may be related to its health and coagulation parameters. Others (85) have shown that the hemostasis process is associated with a change in the dielectric permittivity of blood, which further relates to its coagulation parameters. The same can be explored in relation to the transport properties of blood as well.

APPENDICES

Appendix A

DETERMINATION OF REGIME TRANSITIONS

The average variation of dimensionless front location (X) with dimensionless time (T) is plotted in the log-log scale in Figure 10. A change in the power law behavior in the linear scale manifests itself as a change in slope in the logarithmic scale. Two such changes are observed in Figure 10 – a change of slope from 0.5 to 1 marking the transition from Regime I to Regime II, and another change in slope from 1 to 0.1 corresponding to the transition from Regime II to Regime III. Regime transition points identified from the logarithmic plot have been used to demarcate spreading regimes in Figure 9.

Appendix A (Continued)

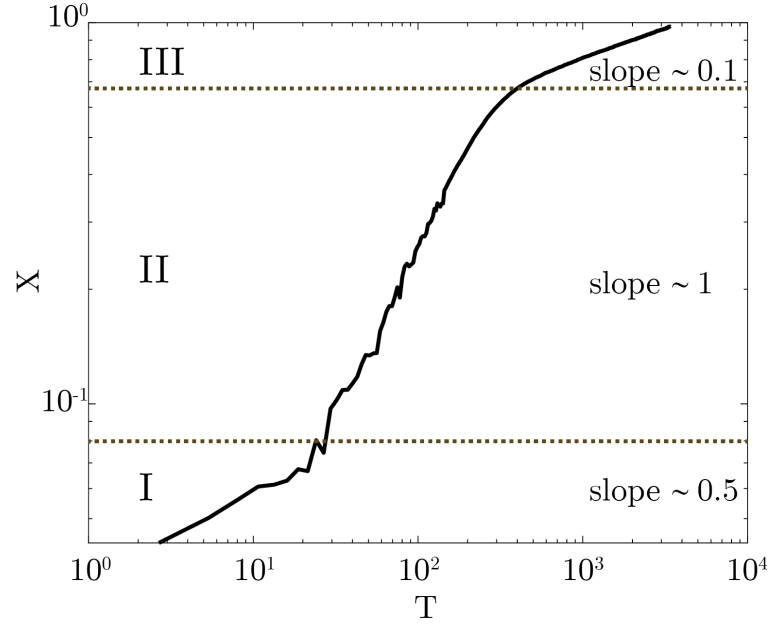


Figure 10. Average dimensionless front location (X) plotted against dimensionless time instant (T) in log-log scale. The changes in slope demarcate the transition from one regime of spreading to the next

Appendix B

EFFECT OF SURFACE TENSION VARIATION

In order to understand the role of surface tension on the transport of liquids on the aforementioned wettability-patterned, diverging tracks, an experiment with a 0.01M aqueous solution of sodium dodecyl sulfate (SDS, Sigma-Aldrich) is performed on a track of the same design as the experiments mentioned in Chapter 3. The surface tension of the solution is 37 mN/m (86; 87), while the viscosity is assumed to be that of water as very little amount of solid material is added. The SDS droplet is observed to move much slower than water due to its surface tension being smaller by approximately a factor of 2. The variation of X with T in the logarithmic scale is presented in Figure 11, along with the average curve for the experiments with water and the aqueous solutions of glycerol. The curves overlap each other satisfactorily, indicating the universal behavior identified in this study appropriately captures the effects of both surface tension and viscosity of the fluid being transported.

Appendix B (Continued)

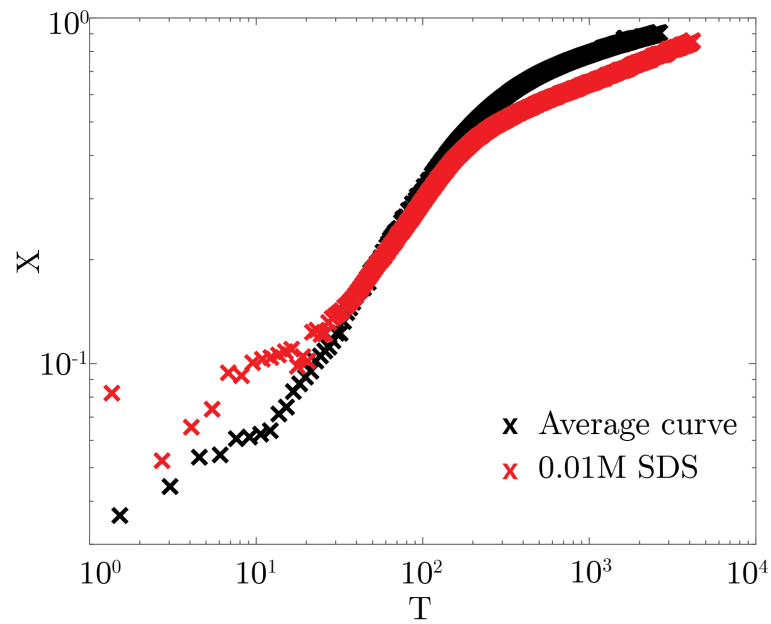


Figure 11. Dimensionless front location, X , plotted against dimensionless time, T , for a 0.01M aqueous solution of sodium dodecyl sulfate (SDS, $\gamma = 37$ mN/m) along with the average variation of X with T for water and the aqueous solutions of glycerol

Appendix C

IMAGE ANALYSIS ALGORITHM

The fundamentals of the image analysis algorithm used in the present work are presented in this section. The commercial software MATLAB is utilized to perform this. Time-lapsed images are obtained from the high-speed video recordings, which were then read using inbuilt commands in MATLAB. MATLAB reads each image as an array of the x-y coordinates of each pixel of the image and the intensity of that pixel. For a particular y coordinate, if all the pixels along that coordinate are sampled for their intensity, an abrupt jump is observed at the pixels corresponding to the spreading liquid front, as demonstrated through a representative snapshot in Figure 12. For each image within a sequence, the x coordinate of this intensity jump, after averaging over a number of y coordinates comprising the liquid volume, is noted and subsequently plotted against time for the entire video sequence to reveal the evolution of the liquid spreading front position with time.

Appendix C (Continued)

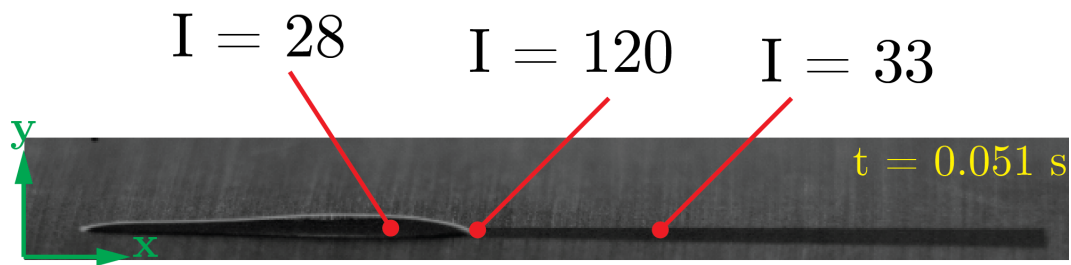


Figure 12. A representative image showing the change of pixel intensity (I) along the spreading liquid volume

Appendix D

PERMISSION FOR IMAGE USED

CITED LITERATURE

1. Whitesides, G. M.: The origins and the future of microfluidics. Nature, 447:368–373, 2006.
2. Bruus, H.: Theoretical Microfluidics. Oxford University Press Inc., New York, 2008.
3. Gervais, L. and Delamarche, E.: Toward one-step point-of-care immunodiagnostics using capillary-driven microfluidics and PDMS substrates. Lab Chip, 9:3330–3337, 2009.
4. Mark, D., Haeberle, S., Roth, G., von Stetten, F., and Zengerle, R.: Microfluidic lab-on-a-chip platforms: requirements, characteristics and applications. Chem. Soc. Rev., 39:1153–1182, 2010.
5. Squires, T. M. and Quake, S. R.: Microfluidics: fluid physics at the nanoliter scale. Rev. Mod. Phys., 77:977–1026, 2005.
6. Haeberle, S. and Zengerle, R.: Microfluidic platforms for lab-on-a-chip applications. Lab Chip, 7:1094–1110, 2007.
7. Puri, I. K. and Ganguly, R.: Particle transport in therapeutic magnetic fields. Annu. Rev. Fluid Mech., 46:407–440, 2014.
8. Foresti, D., Nabavi, M., Klingauf, M., Ferrari, A., and Poulidakos, D.: Acoustophoretic contactless transport and handling of matter in air. Proc. Natl. Acad. Sci., 110(31):12549–12554, 2013.
9. Hourtane, V., Bodiguel, H., and Colin, A.: Dense bubble traffic in microfluidic loops: selection rules and clogging. Phys. Rev. E, 93:032607, 2016.
10. Cong, H., Xu, X., Yu, B., Liu, H., and Yuan, H.: Fabrication of anti-protein-fouling poly(ethylene glycol) microfluidic chip electrophoresis by sandwich photolithography. Biomicrofluidics, 10:044106, 2016.
11. Kaigala, G. V., Lovchik, R. D., and Delamarche, E.: Microfluidics in the “open space” for performing localized chemistry on biological interfaces. Angew. Chem. Int. Ed., 51:11224–11240, 2012.

12. Ghosh, A., Ganguly, R., Schutzius, T. M., and Megaridis, C. M.: Wettability patterning for high-rate, pumpless fluid transport on open, non-planar microfluidic platforms. Lab Chip, 14:1538–1550, 2014.
13. Zhao, Y., Wang, H., Zhou, H., and Lin, T.: Directional fluid transport in thin porous materials and its functional applications. Small, 13:1601070, 2017.
14. Smith, J. D., Dhiman, R., Anand, S., Reza-Garduno, E., Cohen, R. E., McKinley, G. H., and Varanasi, K. K.: Droplet mobility on lubricant-impregnated surfaces. Soft Matter, 9:1772–1780, 2013.
15. Choi, K., Ng, A. H. C., Fobel, R., and Wheeler, A. R.: Digital microfluidics. Annu. Rev. Anal. Chem., 5:413–440, 2012.
16. de Gennes, P.-G., Brochard-Wyart, F., and Quéré, D.: Capillarity and Wetting Phenomena: Drops, Bubbles, Pearls, Waves. Springer-Verlag New York Inc., 2004.
17. Bonn, D., Eggers, J., Indekeu, J., Meunier, J., and Rolley, E.: Wetting and spreading. Rev. Mod. Phys., 81:739–805, 2009.
18. Greenspan, H. P.: On the motion of a small viscous droplet that wets a surface. J. Fluid Mech., 84(1):125–143, 1978.
19. Gau, H., Herminghaus, S., Lenz, P., and Lipowsky, R.: Liquid morphologies on structured surfaces: from microchannels to microchips. Science, 283(5398):46–49, 1999.
20. Feng, X. and Jiang, L.: Design and creation of superwetting/antiwetting surfaces. Adv. Mater., 18:3063–3078, 2006.
21. Seo, J., Lee, S., Lee, J., and Lee, T.: Guided transport of water droplets on superhydrophobic-hydrophilic patterned Si nanowires. ACS Appl. Mater. Interfaces, 3:4722–4729, 2011.
22. Balu, B., Berry, A. D., Hess, D. W., and Breedveld, V.: Patterning of superhydrophobic paper to control the mobility of micro-liter drops for two-dimensional lab-on-paper applications. Lab Chip, 9:3066–3075, 2009.
23. Mertaniemi, H., Jokinen, V., Sainiemi, L., Franssila, S., Marmur, A., Ikkala, O., and Ras, R. H. A.: Superhydrophobic tracks for low-friction, guided transport of water droplets. Adv. Mater., 23:2911–2914, 2011.

24. Schutzius, T. M., Elsharkawy, M., Tiwari, M. K., and Megaridis, C. M.: Surface tension confined (STC) tracks for capillary-driven transport of low surface tension liquids. Lab Chip, 12:5237–5242, 2012.
25. Elsharkawy, M., Schutzius, T. M., and Megaridis, C. M.: Inkjet patterned superhydrophobic paper for open-air surface microfluidic devices. Lab Chip, 14:1168–1175, 2014.
26. Yamada, Y., Ikuta, T., Nishiyama, T., Takahashi, K., and Takata, Y.: Droplet nucleation on a well-defined hydrophilic-hydrophobic surface of 10 nm order resolution. Langmuir, 30:14532–14537, 2014.
27. Piorek, B. D., Lee, S. J., Santiago, J. G., Moskovits, M., Banerjee, S., and Meinhart, C. D.: Free-surface microfluidic control of surface-enhanced Raman spectroscopy for the optimized detection of air molecules. Proc. Natl. Acad. Sci., 104(48):18898–18901, 2007.
28. Seo, J., Lee, S. K., Lee, J., Lee, J. S., Kwon, H., Cho, S. W., Ahn, J. H., and Lee, T.: Path-programmable water droplet manipulations on an adhesion controlled superhydrophobic surface. Sci. Rep., 5:12326, 2015.
29. Kang, H., Heo, Y. J., Kim, D. J., Kim, J. H., jeon, T. Y., Cho, S., So, H. M., Chang, W. S., and Kim, S. H.: Droplet-guiding superhydrophobic arrays of plasmonic microposts for molecular concentration and detection. ACS Appl. Mater. Interfaces, 2017.
30. Martinez, A. W., Phillips, S. T., Whitesides, G. M., and Carrilho, E.: Diagnostics for the developing world: microfluidic paper-based analytical devices. Anal. Chem., 82(1):3–10, 2010.
31. Choudhary, T., Rajamanickam, G. P., and Dendukuri, D.: Woven electrochemical fabric-based test sensors (WEFTS): a new class of multiplexed electrochemical sensors. Lab Chip, 15:2064–2072, 2015.
32. Darhuber, A. A. and Troian, S. M.: Principles of microfluidic actuation by modulation of surface stresses. Annu. Rev. Fluid Mech., 37:425–455, 2005.
33. Yang, J.-T., Yang, Z.-H., Chen, C.-Y., and Yao, D.-J.: Conversion of surface energy and manipulation of a single droplet across micropatterned surfaces. Langmuir, 24:9889–9897, 2008.

34. Bliznyuk, O., Jansen, H. P., Kooij, E. S., Zandvliet, H. J. W., and Poelsema, B.: Smart design of stripe-patterned gradient surfaces to control droplet motion. Langmuir, 27:11238–11245, 2011.
35. Lv, C. and Hao, P.: Driving droplet by scale effect on microstructured hydrophobic surfaces. Langmuir, 2012:16958–16965, 2012.
36. Sommers, A. D., Brest, T. J., and Eid, K. F.: Topography-based surface tension gradients to facilitate water droplet movement on laser-etched copper substrates. Langmuir, 29:12043–12050, 2013.
37. Chaudhury, M. K. and Whitesides, G. M.: How to make water run uphill. Science, 256(5063):1539–1541, 1992.
38. Cira, N. J., Benusiglio, A., and Prakash, M.: Vapor-mediated sensing and motility in two-component droplets. Nature, 519:446–450, 2015.
39. Dos Santos, F. D. and Ondarçuhu, T.: Free-running droplets. Phys. Rev. Lett., 75(16):2972–2975, 1995.
40. Darhuber, A. A., Valentino, J. P., Troian, S. M., and Wagner, S.: Thermocapillary actuation of droplets on chemically patterned surfaces by programmable microheater arrays. J. Microelectromech. Syst., 12(6):873–879, 2003.
41. Chakraborty, M., Ghosh, U. U., Chakraborty, S., and DasGupta, S.: Thermally enhanced self-propelled droplet motion on gradient surfaces. RSC Adv., 5:45266–45275, 2015.
42. Zhao, Y., Liu, F., and Chen, C. H.: Thermocapillary actuation of binary drops on solid surfaces. Appl. Phys. Lett., 99:104101, 2011.
43. Ichimura, K., Oh, S. K., and Nakagawa, M.: Light-driven motion of liquids on a photoreponsive surface. Science, 288:1624–1626, 2000.
44. Linke, H., Alemán, B. J., Melling, L. D., Taormina, M. J., Francis, M. J., Dow-Hygelund, C. C., Narayanan, V., Taylor, R. P., and Stout, A.: Self-propelled Leidenfrost droplets. Phys. Rev. Lett., 96:154502, 2006.
45. Lagubeau, G., Le Merrer, M., Clanet, C., and Quéré, D.: Leidenfrost on a ratchet. Nature Phys., 7:395–398, 2011.

46. Li, Y., He, L., Zhang, X., Zhang, N., and Tian, D.: External-field-induced gradient wetting for controllable liquid transport: from movement on the surface to penetration into the surface. Adv. Mater., 2017.
47. Martinez, A. W., Phillips, S. T., Butte, M. J., and Whitesides, G. M.: Patterned paper as a platform for inexpensive, low-volume, portable bioassays. Angew. Chem. Int. Ed., 46:1318–1320, 2007.
48. Berejnov, V., Djilali, N., and Sinton, D.: Lab-on-chip methodologies for the study of transport in porous media: energy applications. Lab Chip, 8:689–693, 2008.
49. Li, X., Ballerini, D. R., and Shen, W.: A perspective on paper-based microfluidics: current status and future trends. Biomicrofluidics, 6:011301, 2012.
50. Cate, D. M., Adkins, J. A., Mettakoonpitak, J., and Henry, C. S.: Recent developments in paper-based microfluidic devices. Anal. Chem., 87:19–41, 2015.
51. Xing, S., Jiang, J., and Pan, T.: Interfacial microfluidic transport on micropatterned superhydrophobic textile. Lab Chip, 13:1937–1947, 2013.
52. Xu, L.-P., Dai, B., Fan, J., Wen, Y., Zhang, X., and Wang, S.: Capillary-driven spontaneous oil/water separation by superwetable twines. Nanoscale, 7:13164–13167, 2015.
53. Zhang, J. and Han, Y.: Shape-gradient composite surfaces: water droplets move uphill. Langmuir, 23:6136–6141, 2007.
54. Hirai, Y., Mayama, H., Matsuo, Y., and Shimomura, M.: Uphill water transport on a wettability-patterned surface: experimental and theoretical results. ACS Appl. Mater. Interfaces, 9:15814–15821, 2017.
55. Lorenceau, E. and Quéré, D.: Drops on a conical wire. J. Fluid Mech., 510:29–45, 2004.
56. Alheshibri, M. H., Rogers, N. G., Sommers, A. D., and Eid, K. F.: Spontaneous movement of water droplets on patterned Cu and Al surfaces with wedge-shaped gradients. Appl. Phys. Lett., 102:174103, 2013.
57. Nakajima, A., Nakagawa, Y., Furuta, T., Sakai, M., Isobe, T., and Matsushita, S.: Sliding of water droplets on smooth hydrophobic silane coatings with regular triangle hydrophilic regions. Langmuir, 29:9269–9275, 2013.

58. Morrisette, J. M., Mahapatra, P. S., Ghosh, A., Ganguly, R., and Megaridis, C. M.: Rapid, self-driven liquid mixing on open-surface microfluidic platforms. Sci. Rep., 7:1800, 2017.
59. Ghosh, A., Beaini, S., Zhang, B. J., Ganguly, R., and Megaridis, C. M.: Enhancing dropwise condensation through bioinspired wettability patterning. Langmuir, 30:13103–13115, 2014.
60. Mahapatra, P. S., Ghosh, A., Ganguly, R., and Megaridis, C. M.: Key design and operating parameters for enhancing dropwise condensation through wettability patterning. Int. J. Heat Mass Transfer, 92:877–883, 2016.
61. Tan, X., Zhu, Y., Shi, T., Tang, Z., and Liao, G.: Patterned gradient surface for spontaneous droplet transportation and water collection: simulation and experiment. J. Micromech. Microeng., 26:115009, 2016.
62. Koukoravas, T. P., Ghosh, A., Mahapatra, P. S., Ganguly, R., and Megaridis, C. M.: Spatially-selective cooling by liquid jet impinging orthogonally on a wettability-patterned surface. Int. J. Heat Mass Transfer, 95:142–152, 2016.
63. Huang, S., Song, J., Lu, Y., Chen, F., Zheng, H., Yang, X., Liu, X., Sun, J., Carmalt, C. J., Parkin, I. P., and Xu, W.: Underwater spontaneous pumpless transportation of nonpolar organic liquids on extreme wettability patterns. ACS Appl. Mater. Interfaces, 8:2942–2949, 2016.
64. Ody, T., Panth, M., Sommers, A. D., and Eid, K. F.: Controlling the motion of ferrofluid droplets using surface tension gradients and magnetoviscous pinning. Langmuir, 32:6967–6976, 2016.
65. de Gennes, P. G.: Wetting: statics and dynamics. Rev. Mod. Phys., 57(3):827–863, 1985.
66. Šikalo, Š., Wilhelm, H.-D., Roisman, I. V., Jakirlić, S., and Tropea, C.: Dynamic contact angle of spreading droplets: experiments and simulations. Phys. Fluids., 17:062103, 2005.
67. Seveno, D., Vaillant, A., Rioboo, R., Adão, A., Conti, J., and de Coninck, J.: Dynamics of wetting revisited. Langmuir, 25(22):13034–13044, 2009.
68. Sackmann, E. K., Fulton, A. L., and Beebe, D. J.: The present and future role of microfluidics in biomedical research. Nature, 507:181–189, 2014.

69. Vedder, W. and Vermilyea, D. A.: Aluminum + water reaction. Trans. Faraday Soc., 65:561–584, 1969.
70. Zhijia, Y., Yuefei, Y., Yangfeng, L., Shanpeng, S., Subin, H., and Xiuyan, H.: Preparation and characterization of super-hydrophobic surfaces on aluminum and stainless steel substrates. Surf. Rev. Lett., 17(3):375–381, 2010.
71. Yang, J., Zhang, Z., Xu, X., Men, X., Zhu, X., and Zhou, X.: Superoleophobic textured aluminum surfaces. New J. Chem., 35:2422–2426, 2011.
72. Segur, J. B. and Oberstar, H. E.: Viscosity of glycerol and its aqueous solutions. Ind. Eng. Chem. Res., 43(9):2117–2120, 1951.
73. Takamura, K., Fischer, H., and Morrow, N. R.: Physical properties of aqueous glycerol solutions. J. Pet. Sci. Eng., 98-99:50–60, 2012.
74. Quéré, D.: Wetting and roughness. Annu. Rev. Mater. Res., 38:71–99, 2008.
75. Brinkmann, M. and Liposwky, R.: Wetting morphologies on substrates with striped surface domains. J. Appl. Phys., 92(8):4296–4306, 2002.
76. Carlson, A., Bellani, G., and Amberg, G.: Universality in dynamic wetting dominated by contact-line friction. Phys. Rev. E, 85:045302 (R), 2012.
77. Winkels, K. G., Weijs, J. H., Eddi, A., and Snoeijer, J. H.: Initial spreading of low-viscosity drops on partially wetting surfaces. Phys. Rev. E, 85:055301 (R), 2012.
78. Washburn, E. W.: The dynamics of capillary flow. Phys. Rev., XVII(3):273–283, 1921.
79. Darhuber, A. A., Troian, S. M., and Reisner, W. W.: Dynamics of capillary spreading along hydrophilic microstripes. Phys. Rev. E, 64:031603, 2001.
80. Carlson, A., Bellani, G., and Amberg, G.: Contact line dissipation in short-time dynamic wetting. Europhys. Lett., 97:44004, 2012.
81. Tanner, L. H.: The spreading of silicone oil drops on horizontal surfaces. J. Phys. D., 12:1473–1484, 1979.
82. Biance, A. L., Clanet, C., and Quéré, D.: First steps in the spreading of a liquid droplet. Phys. Rev. E, 69:016301, 2004.

- 83. Day, R. F., Hinch, E. J., and Lister, J. R.: Self-similar capillary pinchoff of an inviscid fluid. Phys. Rev. Lett., 80(4):704–707, 1998.
- 84. Chen, A. U., Notz, P. K., and Basaran, O. A.: Computational and experimental analysis of pinch-off and scaling. Phys. Rev. Lett., 88(17):174501, 2002.
- 85. Maji, D., Suster, M. A., Kucukal, E., Sekhon, U. D. S., Sen Gupta, A., Gurkan, U. A., Stavrou, E. X., and Mohseni, P.: ClotChip: A microfluidic dielectric sensor for point-of-care assessment of hemostasis. IEEE Trans. Biomed. Circuits Syst., pages 1–11, 2017.
- 86. Hernáinz, F. and Caro, A.: Variation of surface tension in aqueous solutions of sodium dodecyl sulfate in the flotation bath. Colloids Surf. A, 196:19–24, 2002.
- 87. Stark, A. Y., McClung, B., Niewiarowski, P. H., and Dhinojwala, A.: Reduction of water surface tension significantly impacts gecko adhesion underwater. Integr. Comp. Biol., 54(6):1026–1033, 2014.

VITA

NAME Uddalok Sen

EDUCATION

- Master of Science in Mechanical Engineering, University of Illinois at Chicago, USA, 2017
(expected)
 - Bachelor of Engineering in Mechanical Engineering, Jadavpur University, India, 2014
-

TEACHING EXPERIENCE

- Graduate Teaching Assistant, ME 211 - Fluid Mechanics, Instructor: Prof. Jie Xu,
Department of Mechanical and Industrial Engineering, University of Illinois at Chicago
(January 2016 – May 2016)
-

RESEARCH EXPERIENCE

- Graduate Research Assistant, Micro/Nanoscale Fluid Transport Laboratory, Advisor: Prof.
Constantine M. Megaridis, Department of Mechanical and Industrial Engineering, University
of Illinois at Chicago (January 2016 – Present)
 - Junior Research Fellow, Advisors: Prof. Swarnendu Sen and Prof. Achintya Mukhopadhyay,
Mechanical Engineering Department, Jadavpur University (October 2014 – December 2015)
-

PUBLICATIONS

- *Dynamics of magnetic modulation of ferrofluid droplets for digital microfluidic applications*,
U. Sen, S. Chatterjee, S. Sen, M. K. Tiwari, A. Mukhopadhyay, and R. Ganguly, Journal of
Magnetism and Magnetic Materials, 421, 165 - 176 (2017)

- *Effects of fluid injection on dynamics of flow past a circular cylinder*, U. Sen, A. Mukhopadhyay, and S. Sen, European Journal of Mechanics B/Fluids, 61, 187 - 199 (2017)
- *Dynamic characterization of a ducted inverse diffusion flame using recurrence quantification*, U. Sen, T. Gangopadhyay, C. Bhattacharya, A. Mukhopadhyay, and S. Sen, Combustion Science and Technology (2017)
- *Distribution of impinging liquid jets on wettability-patterned porous polymeric substrates*, U. Sen, S. Chatterjee, P. Sinha Mahapatra, R. Ganguly, R. Dodge, L. Yu, and C. M. Megaridis, ACS Applied Materials and Interfaces (under review)
- *Universality in directional spreading of droplets on wettability-patterned diverging tracks*, U. Sen, S. Chatterjee, R. Ganguly, R. Dodge, L. Yu, and C. M. Megaridis, Langmuir (in preparation)

PATENT APPLICATION

- *A method and device for moving and distributing aqueous liquids at high rates on porous, nonwoven substrates*, C. M. Megaridis, S. Chatterjee, P. Sinha Mahapatra, U. Sen, R. Ganguly, R. Dodge, and L. Yu, US Non-provisional Patent Application 65/013,631 (filed on November 18, 2016)
-